Design And Analysis Of Ultra-Broadband Gain Medium And Waveguide Structure For Terahertz Emission

by

Md. Shahadat Hasan Sohel

Student ID: 0412062252

A thesis submitted in partial fulfillment

for the degree of **Master of Science**

in the

Department of Electrical and Electronic Engineering

Bangladesh University of Engineering and Technology

March, 2015

Declaration

It is hereby declared that this thesis or any part of it has not been submitted elsewhere for the award of any degree or diploma.

_____

(**Md. Shahadat Hasan Sohel**)

Approval Certificate

The thesis titled "Design And Analysis Of Ultra-Broadband Gain Medium And Waveguide Structure For Terahertz Emission" submitted by Md. Shahadat Hasan Sohel, Student ID: 0412062252, Session: April 2012 has been accepted as satisfactory in partial fulfillment of the requirement for the degree of MASTER OF SCIENCE IN ELECTRICAL AND ELECTRONIC ENGINEERING on March, 2015.

Board of Examiners

1._____ Chairman (Supervisor)

Dr. Muhammad Anisuzzaman Talukder
Professor,
Department of EEE, BUET,
Dhaka-1205, Bangladesh

2._____ Member (Ex-Officio)

Dr. Taifur Ahmed Chowdhury
Professor and Head,
Department of EEE, BUET,
Dhaka-1205, Bangladesh

3._____ Member

Dr. Farseem Mannan Mohammedy
Associate Professor,
Department of EEE, BUET,
Dhaka-1205, Bangladesh

4._____ Member (External)

Dr. Ishtiaque M. Syed
Associate Professor,
Department of Physics,
University of Dhaka

Abstract

Quantum cascade laser (QCL) is a promising candidate for comparatively less developed terahertz spectral range. Design-dependent emission frequency and sequential pumping make QCL suitable for Hetero-active region operation, which can emit multiple frequency at the same time. From this multiple frequency emitting QCL, using various tuning techniques, we can achieve a broadband terahertz emission from a single QCL cavity. GaAs based multiple frequency emitting QCL has already been reported, but GaN based QCLs provide significant advantages over traditional GaAs based QCLs due to their higher LO phonon energy. We propose a hetero cavity terahertz GaN based QCL emitting around 1.5 THz, 4 THz, and 7 THz. Using bias tuning, we have achieved an ultra-broadband emission covering a range of 1–10 THz. Current mismatch is an inherent problem in the hetero-structure devices. We calculate the effect of current mismatching in hetero-active structures. We find that both higher and lower current injection results in lower population inversion and hence lower gain, and mismatch of more than 10% results in gain less than typical loss in the cavity. Waveguide design is of significant importance in terahertz range due to the confinement problem of longer wavelength. We design and optimize the waveguide for the QCL using double metal configuration to support the broadband emission of 1–10 THz.

Acknowledgements

I would first like to thank Almighty Allah for His continuous blessings upon me, especially in my educational life, and for bringing me to the position where I am at this very moment.

My completion of this thesis could not have been accomplished without the ceaseless guidance and support of my thesis supervisor, Prof. Dr. Muhammad Anisuzzaman Talukder. He was inspirational in making me come up with the idea of working with broadband quantum cascade laser. During my thesis work, I used the "QCL Simulation Package" developed by him for solving the wavefunctions in quantum cascade lasers. From the very beginning of my thesis till the very end, he guided me thoroughly and gave me ample time to discuss various issues. I consider myself very lucky to have a thesis supervisor like him. And I earnestly hope to maintain an active relation with him for our future research works in the days to come.

Next, I would like to express my gratitude to my teachers and fellow researchers, Asif Ahmed, Golam Md. Imran Hossain, Orchi Hassan, A. F. M. Saniul Haq, Fariah Hayee for their continuous support and help for the last one year.

Finally, my deepest gratitude to my caring, loving, and supportive family. Without their support I would not be able to achieve anything.

Contents

List of Figures

Chapter 1

Introduction

The works of Albert Einstein on "Stimulated Emission" in 1917 laid the foundation for LASER (Light Amplification by Stimulated Emission of Radiation) [1]. But it was not until 1960 that T. H. Maiman first achieved laser action at optical frequencies in Ruby [2]. Shortly after that many types of lasers were invented including solid-state lasers and gas lasers.

Most solid-state and gas lasers utilize narrow optical transitions connecting discrete energy levels. Population inversion is achieved by optical or electrical pumping [3]. In contrast, semiconductor diode lasers, including quantum well lasers use transitions between energy bands. The population inversion is achieved by forward biasing a pn junction, where electrons from conduction band radiatively recombine with holes from valence band across the band gap. The band gap essentially determines the emission wavelength [4]. In addition, as the population inversion is broadly distributed, in accordance with Pauli's principle, between bands having dispersion with opposite curvature, the resulting gain spectrum is

relatively broad. These characteristics have profound implications for the operation of semiconductor lasers. The concepts are schematically shown in Fig. 1.1.

The quest for intersubband wavelength tunable laser started from 1971, when Kazarinov and Suris proposed that light amplification is possible in a transition between two subbands of an energy band in a semiconductor with quantum wells [5]. But due to technological constraints, the physical realization of this type of lasers was delayed. In 1994, Faist *et al.* demonstrated the first intersubband laser, i.e., Quantum Cascade Laser (QCL) at Bell Laboratories [6].

QCL utilizes one type of carrier (unipolar semiconductor laser) and the electronic transitions between conduction band states arise from size quantization in semiconductor heterostructures. The joint density of states of these transitions and the corresponding gain spectrum are therefore narrow and essentially symmetric [6].

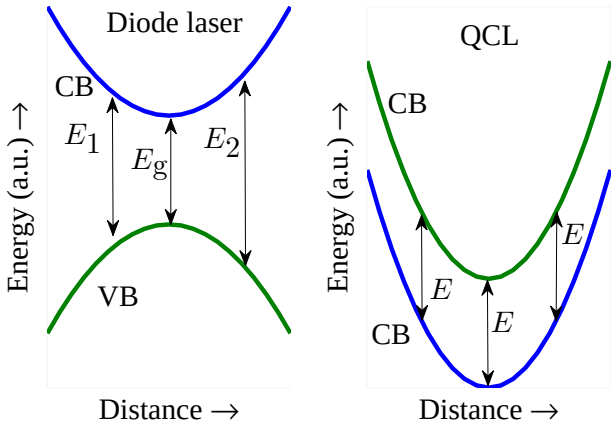

Figure 1.1: Conceptual energy levels involved in transitions for diode lasers and QCLs.

As transitions involve two energy levels from conduction band only, neglecting non-parabolicity, all the emitted photon will have same energy and hence same wavelength as depicted conceptually in Fig. 1.1. Consequently the linewidth for QCL will be narrower. The unique properties of QCLs compared to other semiconductor lasers, such as the ease of generating light at a design wavelength, tunable gain spectrum and ultra-fast carrier dynamics, make them the most important semiconductor lasers that operate today in the mid-infrared and terahertz region [7].

Terahertz (THz) technology can be used in information science, biology, medicine, astronomy, and environmental science [8]. The terahertz frequency range has historically been characterized by a relative lack of convenient radiation sources, detectors and transmission technology [9]. Electrically pumped semiconductor-based sources are particularly attractive because of their operating simplicity and their potential for mass production. THz QCLs are a promising technology for the THz spectral range [10]. QCLs provide the opportunity of wavelength choice and cascading, which can advantageously be used for multi-wavelength emission [11]. From this multiple-wavelength emitting heterogeneous devices, i.e., periods emitting at different wavelengths, tuning techniques can be employed to obtain broadband tunable lasers.

A broadband THz QCL can be attractive for spectroscopic and imaging techniques, widely tunable external cavity devices, and short-pulse generation by active mode locking [12]. Broadband QCL with heterogeneous cascades emitting frequencies between 2.2 to 3.2 THz has been reported [13]. An external-cavity

terahertz quantum cascade laser source tunable between 1.70 and 5.25 THz has recently been reported [14]. In refs. [13] and [14], GaAs based material system has been used, which has a LO phonon energy of ~32 meV. This poses a maximum limit on the emission frequency theoretically at around 7 THz. Practically, however, temperature effects limits the emission frequency to a much lower value. At higher temperature, electrons in lower levels, by thermal excitation can be backfilled to lower lasing level and hence decrease the population inversion, and electrons in the upper lasing level can acquire sufficient in-plane kinetic energy to emit LO phonons and relax to the lower lasing level in a non-radiative manner [15]. Practically demonstrated emission is up to 5 THz [14].

Alternatively, relatively less explored GaN based material system has the potential to provide broader THz frequency range and better temperature performance. The LO phonon energy of GaN is (~90 meV), so the theoretical limit is extended up to 21 THz [16]. There are important applications in the extended terahertz range between 5–10 accessible by GaN. The constituents of DNA and RNA like nucleobases, nucleosides, deoxynucleosides, and nucleotides have quite different characteristics spectral pattern in the 5–10 THz range [17]. The whole 1–10 THz range can be very important in communication, because this band is completely unallocated in the spectrum for communication [18].

Heterogenous device structures inherently suffers from current mismatch due to different current generation in each type of structures. Each structure generates current of its own for a specific bias, which will usually be different for different structures. As a result there will be mismatch between current of different struc-

tures. The current will be limited by the minimum current generated between all the structures [19]. The current mismatch results in lower gain and hence reduced output power. In Ref. [20], Geiser et. al. reported that if the current in two hetero-structures are different, there will be reduction in the population inversion. But no detail analysis on how the current mismatch affects the population inversion or gain of the laser is not reported till date.

In this work, we propose a GaN based hetero-active region ultra-broadband quantum cascade laser which consists of three different active regions. The three active regions are designed to emit terahertz frequency around 1.5 THz, 4 THz and 7 THz. We have used bias tuning and achieved a broadband tunability of 1–10 THz. We discuss the detail opto-electronic properties of the proposed ultra-broadband QCL. We calculate the effect of current mismatch, which can significantly degrade the performance of hetero structures. We find that if the current mismatch is more than 10%, the population inversion decreases to a low value that results in lower gain resulting in diminishing of emission. We also investigate the performance of waveguides for the broad emission range.

Our proposed ultra-broadband QCL structure emits in the terahertz range of 1–10 THz. In this range, the emission will have significantly longer wavelength than the typical mid-IR emission from QCL. So, special types of waveguide design is necessary to accommodate the longer wavelength. Two types of waveguides are commonly used at present for the terahertz QC lasers: the semi-insulating surface-plasmon (SI-SP) and the metal-metal (MM) waveguide [9]. Traditionally, long-wavelength quantum-cascade lasers exploit the surface plasmon mode

at the interface between two materials with dielectric constants of opposite sign (normally a metal and a semiconductor) to achieve a tight optical confinement with low absorption losses [21]. At the frequencies of our designed QCL, however, a surface-plasmon waveguide results in a small overlap of the optical mode with any active region of reasonable thickness [22]. MM waveguides with metal layer at both sides, provides excellent confinement of modes within the waveguide. MM waveguide design, compared to the SI-SP waveguide design, empirically provides the best temperature performance for terahertz QCLs in the desired emission frequency range [23]. We calculate the performance for both types of waveguides and optimize the parameter for best performance. We find that double metal waveguide with copper cladding provides the best result in terms of higher confinement and lower threshold gain. We also optimize the waveguide structure to achieve best output emission.

The rest of the thesis is organized as follow:

Chapter 2 discusses the detail of the proposed ultra-broadband QCL and its design considerations. It also discusses the materials used for the design and the advantages for using them.

Chapter 3 describes the electrical properties of the proposed ultra-broadband QCL. It discusses theoretical modeling and presents the results of carrier transport, I-V characterization, material modeling, and finally the gain of the emission.

Chapter 4 discusses the optical properties of the proposed QCL. It describes the

method of confinement of the generated light within the waveguide, effects of loss within the cavity, shape of the modes inside the cavity, and final output emission.

Chapter 5 presents the summary of the results with scope for further work and concludes the thesis.

Chapter 2

Proposed Ultra-broadband Terahertz Quantum Cascade Laser

We propose a hetero-active region gain medium, which consists of repetition of three different gain medium. The structure is schematically shown in the Fig. 2.1. For convenience of description, we will call the three structures as S_1, S_2, and S_3. Each of the gain medium is designed to emit a specific frequency in the Terahertz range. At a specific bias, we will have three frequency emission. With bias variation, we will have change in energy levels and hence, the emission frequency can be varied between the two limiting value of bias, up to which population inversion can be achieved. If we can design the structure such that the emissions will have sufficient gain from all the mediums, we will have sustained output emission over a wide range. If the emission from all the three structures can be provided with sufficient gain, we can achieve a broadband emission.

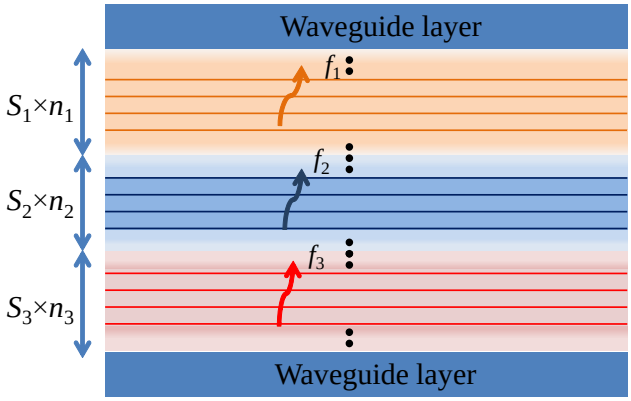

Figure 2.1: Schematic of the overall design structure. Here, structures S_1, S_2, and S_3 periods are repeated n_1, n_2, and n_3 times respectively and emit f_1, f_2, and f_3 frequency respectively.

2.1 Design Strategy

Each gain medium is composed of GaN well and AlGaN barrier. The active regions are of resonant phonon type. In this type of design, as shown in Fig. 2.2, collector state E_0 is designed to be below the lower radiative state E_1 by approximately LO phonon energy, so that electrons after transition from upper lasing level E_2 to the lower lasing level E_1 state, will scatter very quickly into the collector E_0 state by emitting an LO-phonon. This type of structure offers two advantages. Firstly, when the energy levels between collector state (E_0) and lower state (E_1) are separated by at least E_{LO}, depopulation is extremely fast, and is not particularly dependent on either temperature or the electron distribution. Secondly, the large energy separation provides intrinsic protection against thermal backfilling from collector state (E_0) into upper state (E_1) [24].

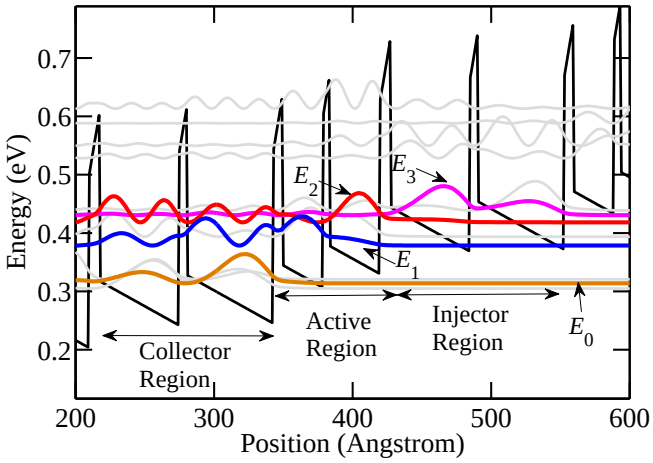

Figure 2.2: Bandstructure and the moduli squared of the relevant wave functions for one and a half period of S_1 structure. The upper lasing level (E_2), lower lasing level (E_1), injector ground (E_3), and the first collector level (E_0) are shown with bold line.

We propose to use a GaN-based system with large LO-phonon energy of 90 meV for THz QCLs. The advantages are threefold. First, the large LO-phonon energy in a GaN-based system can reduce the thermal population of the lower laser state. Second, ultrafast LO-phonon scattering in GaN/AlGaN quantum wells can be used for the rapid depopulation of the lower laser state. Third, the large LO-phonon energy can also increase the lifetime of the upper laser state by reducing the relaxation of electrons with higher in-plane kinetic energy via emission of a LO-phonon [25].

2.2 Gain Medium

S_1 is designed to emit around 7.2 THz, S_2 is designed to emit around 4.3 THz, and S_3 is designed to emit around 1.7 THz. GaN based quantum structures must have

zero overall potential within a period to ensure the stability of the structure. Here, each gain medium is so designed that they satisfy the periodic boundary condition [26]

$$\sum_j l_j E_j = 0, \tag{2.1}$$

where l_j is the length of a GaN well or AlGaN barrier and E_j is the internal electric field.

All three gain medium period S_1, S_2, and S_3 consist of four quantum wells. The layer sequence for one period of S_1 is (in nm) 5.7/ **0.62**/ 6.18/ **0.73**/ 2.85/ **0.52**/ 3.6/ **0.83**, beginning from an injection layer for a depopulation layer. The structure and the corresponding waveufunctions are shown in Fig. 2.2 The layer sequence for one period of the S_2, as shown in Fig. 2.3 is (in nm) 5.7/ **0.62**/ 6.18/ **0.73**/ 2.8/ **0.52**/

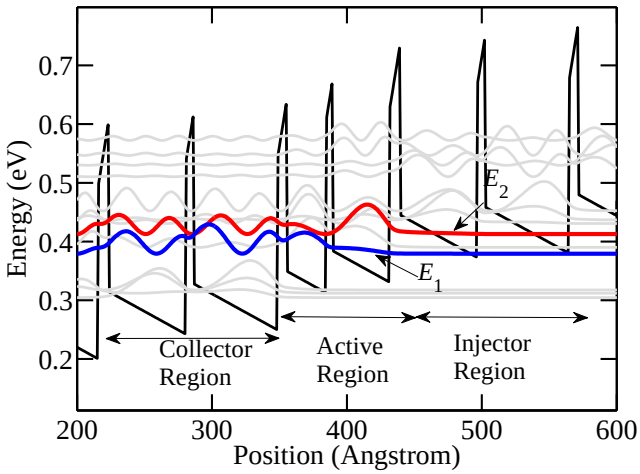

Figure 2.3: Bandstructure and the moduli squared of the relevant wave functions for one and a half period of S_2 structure. The upper lasing level (E_2) and lower lasing level (E_1) are shown with bold line.

4.2/ **0.83**, beginning from an injection layer for a depopulation layer. The normal and bold scripts denote the GaN wells and the AlGaN barriers, respectively. In both S_1 and S_2, the 6.18 nm thick GaN wells are n-doped to 2×10^{11} cm^{-2}. The corresponding wavefunctions for S_1 and S_2 are shown in Figs. 2.2 and 2.3.

S_1 and S_2 have same injector region design, but the active region design is different. The active region of S_1 consists of two quantum wells of 2.85 nm and 3.6 nm, whereas the two quantum wells in S_2 are of 2.8 nm and 4.2 nm. The wider active region results in a lesser energy difference between two lasing levels (marked as E_1 and E_2 in Fig. 2.3) and hence we get a smaller frequency output in S_2 than in S_1. The modification of the other active region layers results in better electron transition to create sufficient population inversion in S_2.

Both the active region and injector structures are different for S_3 as shown in

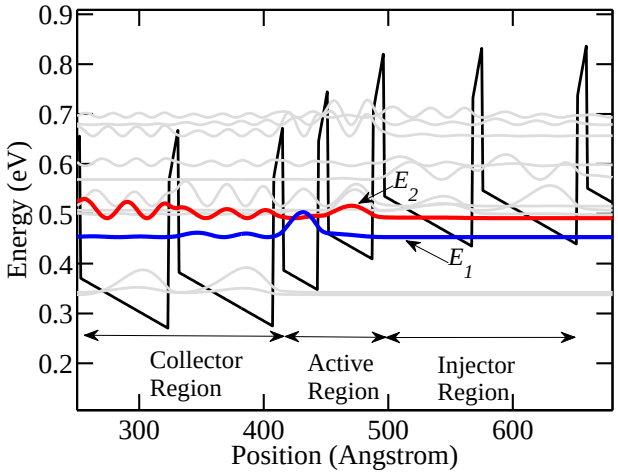

Figure 2.4: Bandstructure and the moduli squared of the relevant wave functions for one and a half period of S_3 structure. The upper lasing level (E_2) and lower lasing level (E_1) are shown with bold line..

Fig. 2.4 with the corresponding wavefunctions. The layer sequence for one period of the structure S_3 is (in nm) 7.1/ **0.8/** 7.6/ **0.8/** 2.8/ **0.8/** 3.6/ **0.9**, beginning from an injection layer for a depopulation layer. The 7.6 nm thick GaN well is n-doped to 5×10^{10} cm^{-2}. Here, S_3 has a different design for injector region than that of S_1 and S_2. We also note that the barrier width is changed. The injector wells are 7.1 nm and 7.6 nm in S_3, instead of 5.7 nm and 6.18 nm in S_1 and S_2. The active region barrier is also changed to 0.8 nm from 0.52 nm. These changes result in a much smaller emission frequency, due to smaller energy difference between between the lasing levels (marked as E_1 and E_2 in Fig. 2.4) than that of the other two structures.

In a hetero structure design, all the structures cannot carry the same current. Say, S_1, S_2, and S_3 will have I_1, I_2, and I_3 current. Total device current will be defined by any of the currents S_1, S_2, or S_3. So, there will be some kind of bottleneck due to current mismatch. For smooth flow of carriers, we need a special transitional structure for electron transition from last period of S_2 to first period of S_3. We have designed a transitional injector region as the to match the energy levels, which has the injector level layer sequence as (in nm) 2.85/**0.7**/3.8.

Chapter 3

Ultra-broadband Terahertz Quantum Cascade Laser Electrical Properties

Electrical properties of a laser is one of the most important characteristics of it. It determines the performance of the gain medium of the laser. So, we have to analyze the electrical properties of the proposed ultra-broadband Quantum Cascade Laser to determine the performance of the QCL. To determine the electrical performance of the proposed structure, we have to analyze its carrier transport, I-V characteristics, and gain at different conditions.

3.1 Theoretical Modeling

We have constructed a theoretical model to calculate the carrier transport and gain of the QCL at a specific bias and temperature. Using that model, we have analyzed the effects of changing various parameters on the gain of the emission.

3.1.1 Gain Spectrum

We have three different gain medium in our proposed design. To obtain the gain of the overall emission, we have to consider each gain medium individually and then combine their effects. To find the the output emission wavelength from each gain medium, first we must find the mode that will lase. The axial modes that are supported by a laser cavity of length L are given by [27]

$$f = m\frac{c}{2nL}, \tag{3.1}$$

where c is the speed of light, n is the index of refraction, and m is an integer that denotes mode number. In practice, a number of axial modes lie within the gain linewidth of QCLs. However, in QCLs, which have a homogenously broadened gain medium, the mode that first experiences gain greater than loss becomes the sustained mode in the cavity.

Now, to calculate gain spectrum for each gain medium individually, we need to calculate the gain of the axial mode supported by each gain medium. The peak modal gain of a QCL for radiative transition from subband j to subband i is given

by [28]

$$G_M = \frac{4\pi q^2}{\varepsilon_0 n \lambda} \frac{z_{ij}^2}{2\gamma_{ij} L_p} (n_j - n_i), \tag{3.2}$$

where q is the charge of an electron, ε_0 is the permittivity of free space, n is the index of refraction, λ is the transition wavelength, $2\gamma_{ij}$ is the full width at half maximum (FWHM) linewidth, z_{ij} is the dipole matrix element, L_p is the length of a period, Γ is the confinement factor, and n_i, n_j are the carrier densities in subbands i and j, respectively. The gain spectrum is found by multiplying the peak modal gain by the Lorentzian lineshape, L_{ij}, given by

$$G = G_M L_{ij}. \tag{3.3}$$

The calculation of the gain spectrum using Eq. (3.2) requires the determination of the dipole matrix element z_{ij} between the levels i and j, the FWHM linewidth γ_{ij} for the transition from level i to level j, and the carrier densities in the subbands i and j. The calculations of z_{ij}, γ_{ij}, n_i and n_j are described in the following.

The dipole matrix element z_{ij} represents the strength of an optical transition between subbands i and j. The dipole matrix element is given by [28]

$$z_{if} = \frac{\hbar}{2(E_f - E_i)} \left\langle \psi_i \middle| p_z \frac{1}{m^*(E_i, z)} + \frac{1}{m^*(E_j, z)} p_z \middle| \psi_z \right\rangle, \tag{3.4}$$

where the energy dependent effective mass is given by

$$m^*(E) = m^*(E = 0) \left(1 + \frac{E - V}{E_G} \right), \tag{3.5}$$

where E is the electron energy, V is the energy of the conduction band edge, and E_G is the energy gap between the conduction band and valence band.

The linewidth for the radiative transition between subbands i and j is given by

$$2\gamma_{ij} = \hbar\left(\frac{1}{\tau_{i\to j}} + \frac{1}{\tau_{i\to i}} + \frac{1}{\tau_{j\to j}}\right), \tag{3.6}$$

where $\tau_{i\to j}$ is the lifetime of electrons due to inter-subband scattering between subbands i and j and $\tau_{i\to i}$ is the intra-subband scattering lifetime in subband i. Among the different inter subband scattering mechanisms in QCLs, electron-LO phonon scattering rate is greater than that of other mechanisms by at least an order of magnitude [29]. However, electron scattering rate due to interface roughness within the subbands in QCLs becomes significant [30]. In this work, we calculate the linewidth considering the electron scattering due to LO phonon and interface roughness and this approach agrees well with experiments [31].

Linewidth for the LO phonon scattering and interface roughness is calculated as [31]

$$2\gamma_R = (\pi m^*/\hbar^2)\Delta^2\Lambda^2\delta\mathrm{U}^2\sum_k[\psi_i^2(z_k) - \psi_j^2(z_k)]^2, \tag{3.7}$$

where $\psi_i(z_k)$ is the wave function of the state i for the carriers with the effective mass m^* at the interface $z = z_k$ and δU is the conduction band offset. The interface parameter product $\Delta\Lambda$ is fixed for a given set of epitaxial growth parameters.

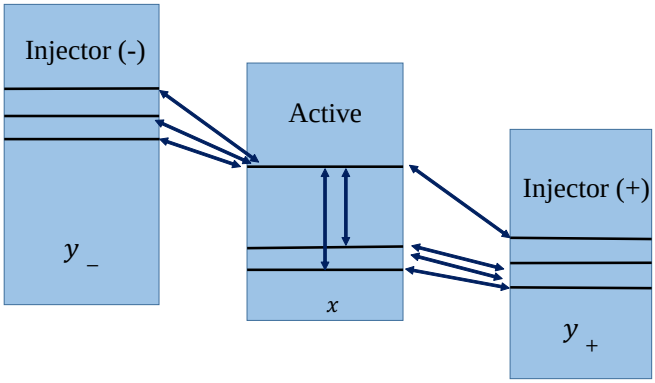

Figure 3.1: Schematic illustration of the carrier transport model

3.1.2 Carrier Transport

To solve for the steady-state carrier density, we have taken one active region and two injector regions preceding and following the active region. Figure 3.1 shows the illustration of carrier transport. At the beginning of the simulation, we distribute the total number of carriers equally among the energy levels in the injector region. The carrier densities are redistributed in the injector and active region energy levels as the rate equations are solved with respect to time. Finally, we get steady-state carrier densities in a time scale greater than the scattering lifetimes of the states. The rate equations that we solve are given by [32]

$$\frac{dn_{A,x}}{dt} = \sum_{x' \neq x} \frac{n_{A,x'}}{s_{x'x}} + \sum_{y_-} \frac{n_{I,y_-}}{s_{y_-x}} + \sum_{y_+} \frac{n_{I,y_+}}{s_{y_+x}} - \sum_{y_-} \frac{n_{A,x}}{s_{xy_-}} - \sum_{x' \neq x} \frac{n_{A,x}}{s_{x'x}} - \sum_{y_+} \frac{n_{A,x}}{s_{xy_+}} \quad (3.8a)$$

$$\frac{dn_{I,y_-}}{dt} = \sum_{y'_-\neq y_-} \frac{n_{I,y'_-}}{s_{y'_-y_-}} + \sum_x \frac{n_{A,x}}{s_{xy_+}} + \sum_x \frac{n_{A,x}}{s_{xy_-}} - \sum_x \frac{n_{I,y_-}}{s_{y_-x}} - \sum_x \frac{n_{I,y_+}}{s_{y_+x}} - \sum_{y'_-\neq y_-} \frac{n_{I,y_-}}{s_{y_-y'_-}} \tag{3.8b}$$

$$\frac{dn_{I,y_+}}{dt} = \sum_{y'_+\neq y_+} \frac{n_{I,y'_+}}{s_{y'_+y_+}} + \sum_x \frac{n_{A,x}}{s_{xy_+}} + \sum_x \frac{n_{A,x}}{s_{xy_-}} - \sum_{y'_+\neq y_+} \frac{n_{I,y_+}}{s_{y_+y'_-}} - \sum_x \frac{n_{I,y_+}}{s_{y_+x}} - \sum_x \frac{n_{I,y_-}}{s_{y_-x}}, \tag{3.8c}$$

where the parameter n is the carrier density in the energy levels. Subscripts A and I denote active and injector regions, respectively. Indices x and y indicate the levels in the active and injector regions, respectively. Subscripts - and + denote a quantity in the injector region that precedes and follows the active region, respectively. The parameter s_{xy} is the scattering time between levels x and y. In this approach, we do not solve the rate equations in k-space. However, we calculate the scattering rates assuming that the carriers are distributed at high in-phase k-values, which depends on the temperature and carrier density of the subband. Then the scattering rates are calculated taking the average assuming Fermi distribution of the carriers.

Now, we need to consider the overall carrier transport of the hetero-active region design. To do this, first we have calculated current for each structure for different bias. The total conductance of a quantum cascade structure can be described as the sum of the partial conductance of different paths in parallel, each of these paths being an intersubband phonon-mediated transition from one subband in a cascade "A" (E_i) to another subband in the next cascade "B" (E_j). The concept is

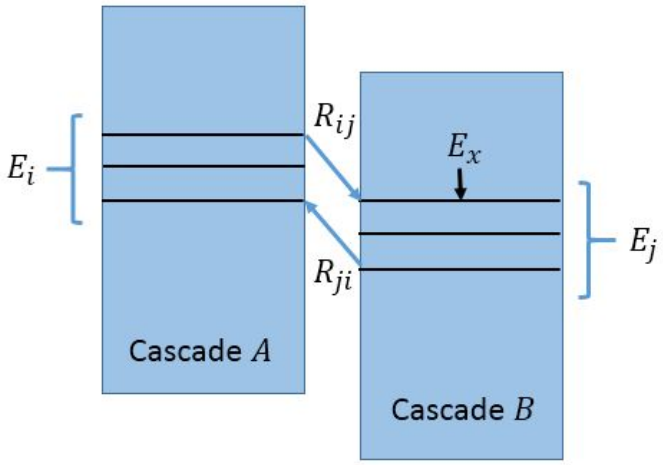

Figure 3.2: Schematic illustration of the current calculation for cascaded structure.

schematically shown in Fig. 3.2. The total current density can then be expressed as:[19]

$$J = e \sum_{i \in A} \sum_{j \in B} \Big(R_{ij}(V) - R_{ji}(V) \Big), \tag{3.9}$$

where e is the electronic charge and R_{ij} is the global electronic transfer rate from subband i to subband j, which depends on the applied bias V. Here, R_{ij} is equal to the inverse of scattering time between levels E_i and E_j.

Now, for hetero-active region structure, current between two different gain medium may vary. To study the effect of current mismatch, we have modified the steady state equation to make the injection in a period variable and controlled by a current which will be defined by the previous gain medium. To incorporate this effect, we have substituted the term $\sum_x n_{A,x}/s_{xy_+}$ in Eq. (3.8b), which represents the injection of electrons from previous active region, with electrons resulting from current

injection from previous gain medium. Now, the modified Eq. (3.8b) becomes

$$\frac{dn_{I,y_-}}{dt} = \eta_x \frac{J}{q} + \sum_{y'_- \neq y_-} \frac{n_{I,y'_-}}{s_{y'_- y_-}} + \sum_x \frac{n_{A,x}}{s_{x y_-}} - \sum_x \frac{n_{I,y_-}}{s_{y_- x}} - \sum_x \frac{n_{I,y_+}}{s_{y_+ x}} - \sum_{y'_- \neq y_-} \frac{n_{I,y_-}}{s_{y_- y'_-}}, \quad (3.10)$$

where η_x is a factor which determines the fraction of the carrier from the current injection goes to the energy level x. It is found from, as illustrated in Fig. 3.2, ratio of the electronic transfer rate from all energy levels (E_i) of previous cascade structure "A" to a specific energy level, E_x in cascade "B", to sum of electronic transfer rate from all energy levels (E_i) in cascade "A" to all energy levels (E_j) to cascade "B". The equation can be written as

$$\eta_x = \frac{\sum_{i \in A} R_{ix}}{\sum_{i \in A} \sum_{j \in B} R_{ij}} \quad (3.11)$$

3.1.3 Material Modeling

We have considered electrical and optical properties of GaN based materials. The temperature dependent bandgap energy E_g can be found by methods described in [33]. The polarization, which is responsible for internal electric field of GaN based materials consists of spontaneous and piezoelectric components. The spontaneous polarization in C/m^2 for the $Al_xGa_{1-x}N$ alloy as function of the Al content x can be approximated by [34]

$$P_{\text{spAlGaN}}(x) = -0.090x - 0.034(1 - x) + 0.021x(1 - x). \quad (3.12)$$

Wurtzite group III nitrides exhibit an additional piezoelectric polarization P_{piezo}

when stress is applied. The piezoelectric polarization can be written as

$$P_{\text{piezo}} = 2\frac{a - a_0}{a_0}\left(e_{31} - e_{33}\frac{C_{13}}{C_{33}}\right). \tag{3.13}$$

The parameters used for the calculation of polarization are taken from references [33] and [35].

The existence of both built-in polarization fields in wurtzite III Nitride semiconductors leads to energy band bending. The electrostatic fields in each layer j-th as a result of total polarization fields can be expressed as [26]

$$E_j = \frac{\sum_k (P_k - P_j)\frac{l_k}{\epsilon_k}}{\epsilon_j \sum_k \frac{l_k}{\epsilon_k}}, \tag{3.14}$$

where P is the total macroscopic polarization, ϵ is the static dielectric constant, and l is the thickness of each layers (k-th, j-th). The subscripts k and j correspond to the k-th and j-th layers.

To ensure zero average electric field in the layers, note that the electric field expression in (3.14) needs to satisfy the periodic boundary conditions as follows: [26]

$$\sum_j l_j E_j = 0, \tag{3.15}$$

where l_j is the length of a GaN well or AlGaN barrier and E_j is the internal electric field.

3.2 Results and discussions

We have calculated gain spectrum for combined emission of the three gain mediums. We also calculated the carrier transport and effect of current mismatch in different gain medium on output emission. We have used bias tuning technique to achieve a broad range of frequency. We calculated the emission tuning range due to the changes in bias. We present the results of electrical property analysis in this section.

3.2.1 Gain Spectrum

We have calculated the overall gain spectrum for the proposed design for different temperature. The calculated gain spectrum is shown in Fig. 3.3 for 100 K and 150 K. We note that we have emission of three frequencies in the terahertz range, from three different gain medium. The emission from S_1 is at 7.2 THz, S_2 is at 4.3 THz, and S_3 is at 1.7 THz. We note that, the gain spectrum at higher temperature i.e. 150 K, is significantly lower. This can be attributed to decrease in the population gain from thermal backfilling at high temperature.

3.2.2 Effect of Current Mismatch

We have calculated the currents for each of the structures for various bias using Eq. (3.9), which is shown in Fig. 3.4. We note that the current density for S_1 and S_3 is close to each other at lower bias, but the difference slowly increases with bias increase. Whereas, the current density difference for S_1 and S_2 is higher at lower temperature, which decreases with bias increase.

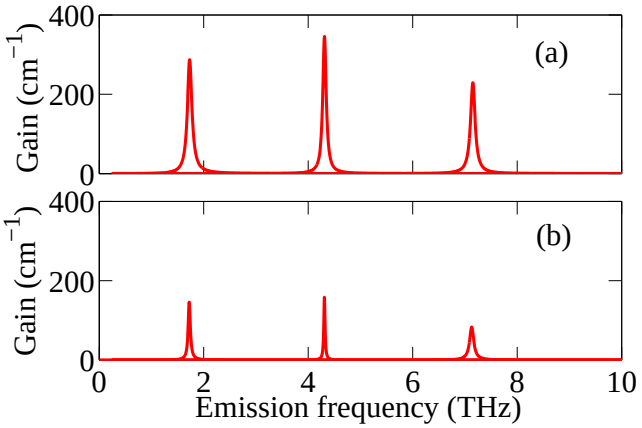

Figure 3.3: Overall gain of the proposed design for (a) 100 K and (b) 150 K temperature

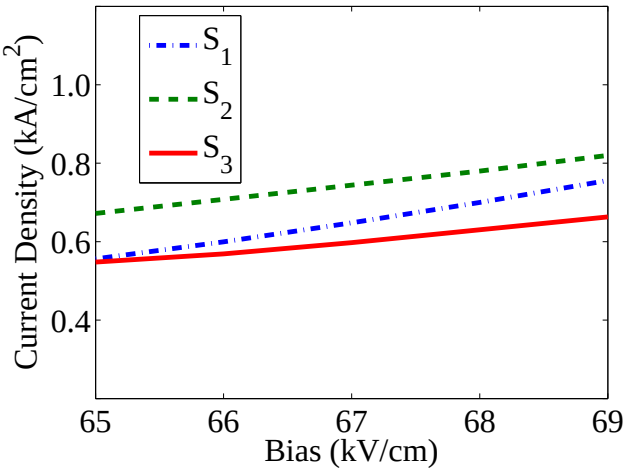

Figure 3.4: Variation in current density with respect to bias change.

To analyze the effect of this mismatch, we have considered a variable injection of current with specific mismatch to a particular gain medium and calculated the steady state population of all energy states. We discuss the effect of current mismatch between S_1 and S_2. The carrier density for upper and lower lasing level of

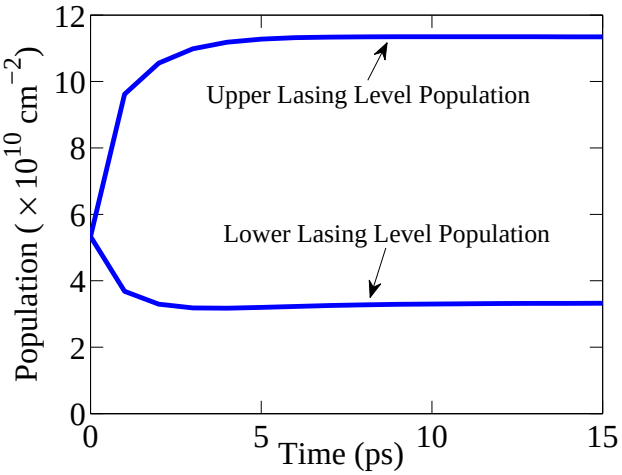

Figure 3.5: Calculated population density for upper and lower lasing level of S_2 without any current mismatch.

S_2 gain medium is shown in Fig. 3.5, which shows population inversion of around 7×10^{10} cm^{-2}. Figure 3.6 shows that for higher injected current the population of the lower lasing level increases, but the upper lasing level population remains almost unchanged, which results in lower population inversion. For a 10% higher

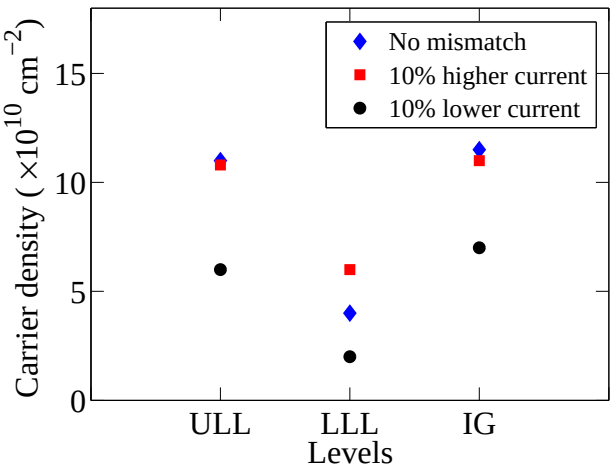

Figure 3.6: Variation of carrier density in upper lasing level (ULL), lower lasing level (LLL) and injector ground (IG) for different current mismatch.

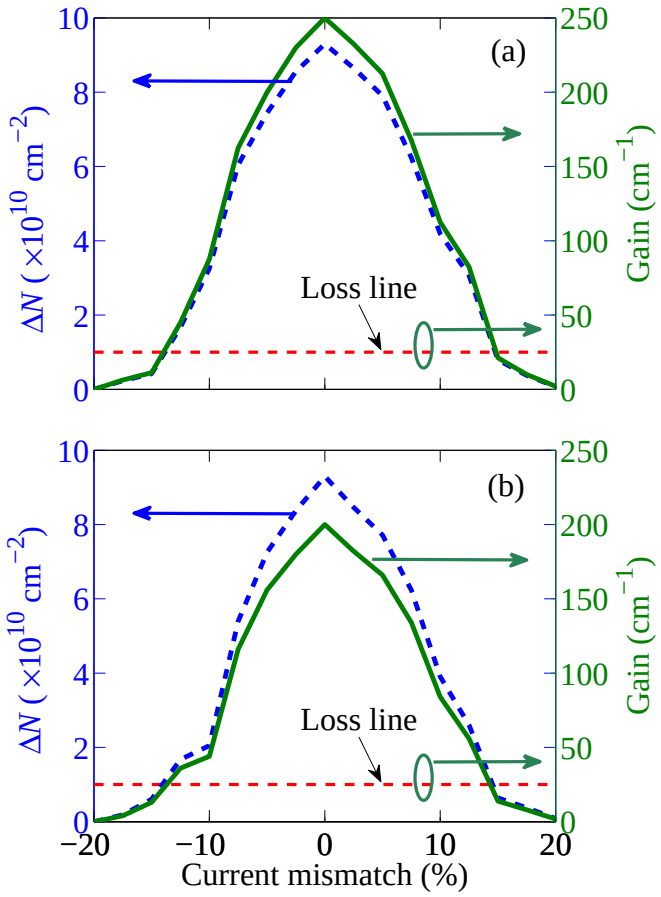

Figure 3.7: Effect on population inversion and gain due to current mismatch (a) From current injection in S_2 from S_1 and (b) From current injection in S_3 from S_2.

current injection for the same gain medium, population inversion is around $4{\times}10^{10}$ cm^{-2}. For lower current injection, both the population of upper and lower level decreases by almost same factor, which results in a population inversion lowered by the same factor. For a 10% lower current injection for the same gain medium, the population inversion is around 3.5×10^{10} cm^{-2}.

We note that for both higher and lower injection of current, the population inver-

sion decreases. As we can see from Eq. (3.2), gain is directly related to population inversion, with the decrease in population inversion, gain will also decrease. The calculated variation of population inversion and gain for different current mismatch from current injection in S_2 from S_1 and from current injection in S_3 from S_2 are shown in Fig. 3.7. As we can see for both cases, the gain reduces to a typical loss in the cavity if the current mismatch is more than 10%.

3.2.3 Tuning with Bias

We have found that the emission frequency can be tuned by varying the bias voltage. We have calculated the variation in gain and emission with bias variation. Bias variation within 65–69 kV/cm, results in sufficient gain with low current mismatch to overcome the loss in the cavity. The tuning with bias variation is shown in Fig. 3.8. We have been able to cover most of the frequencies of a wide range of 1–10 THz with this bias variation tuning technique.

We note that the emission from S_1 starts from 6.3 THz at 65 kV/cm bias with a very low gain. With the increase in bias, the emission frequency increases and we have a higher gain up to 7.7 THz. The energy level difference between the lasing level increases from 26 meV (corresponding to 6.3 THz) up to 31.9 meV. Then there is a change in the lasing level and the emission frequency also changes to 8.4 THz, where the gain also starts to decrease. We have emission from 6.3 THz to 8.6 THz within the bias variation range from 65–69 kV/cm, which covers a range of 2.3 THz.

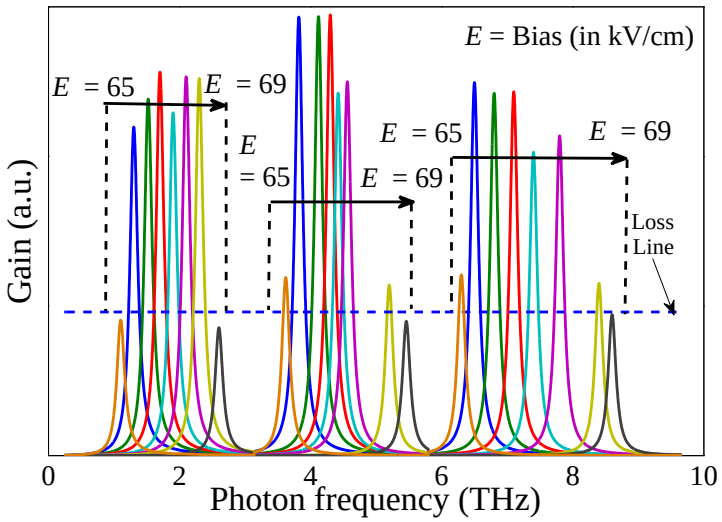

Figure 3.8: Range of frequency tuning with bias variation.

In a similar pattern, the emission from S_2 starts from 3.6 THz at 65 kV/cm bias with a very low gain. With the increase in bias, the emission frequency increases and we have a higher gain up to 4.6 THz. The gain starts to fall around 5.2 THz. We have emission from 3.6 THz to 5.5 THz within the bias variation range from 65–69 kV/cm, which covers a range of 1.9 THz.

Next, the emission from S_3 starts from 1.1 THz at 65 kV/cm bias with a very low gain. With the increase in bias, the emission frequency increases and we have a higher gain up to 2.3 THz. The gain starts to fall sharply around 2.6 THz We have emission from 3.6 THz to 5.5 THz within the bias variation range from 65–69 kV/cm, which covers a range of 1.5 THz.

Chapter 4

Ultra-broadband Terahertz Quantum Cascade Laser Optical Properties

The terahertz emission light confinement is of significant importance. Terahertz emission has significantly longer wavelength than the traditional mid-IR emission for QCL. Due to longer wavelength, THz QCL waveguide design is quite different and challenging. Typically, terahertz QCLs use semi-insulating surface plasmon (SI-SP) and Metal-Metal (MM) waveguide. The SI-SP waveguide involves the growth of a thin (0.2-0.8 μm thick) heavily doped layer underneath the active region, but on top of a semi-insulating substrate. The alternative to the SI-SP, the MM waveguide, uses metal layers, which are placed immediately above and below the epitaxial active region by metallic wafer-bonding to obtain a mode almost completely confined to the active region.

4.1 Theoretical Modeling

We have developed a model to analyze the response of waveguide, which will support the emission from the proposed structure to get the combined effect of waveguide and hetero-active region gain medium.

4.1.1 Wave Equation Analysis

To find the response of the waveguide we have to solve the Maxwell's wave equation with spatial variation modified for laser medium to include the effects of gain and loss. To solve the equation directly in time domain takes up a huge simulation time. So we use Finite-Difference Time-Domain method to solve the Maxwell equation, where the Electric field is discretized in time domain and solved numerically. This method gives sufficient accuracy and relatively lower computation time. Each gain medium is modeled in the FDTD simulation as four level system. The light is modeled with a broadband source, ranging from 1–10 THz, which injects light in gain mediums. The variation of the parameters for FDTD is shown in Fig. 4.1.

The Maxwell's equation for electric field in a laser medium assuming a slowly varying envelope is given by

$$\frac{n}{c}\frac{\partial E_{\pm}}{\partial t} = \mp\frac{\partial E_{\pm}}{\partial z} + (g - l)E_{\pm}. \tag{4.1}$$

Here, E is the electric field, n is the refractive index of the medium, g is the gain of the laser medium and l is the cavity loss. Cavity loss is determined from the

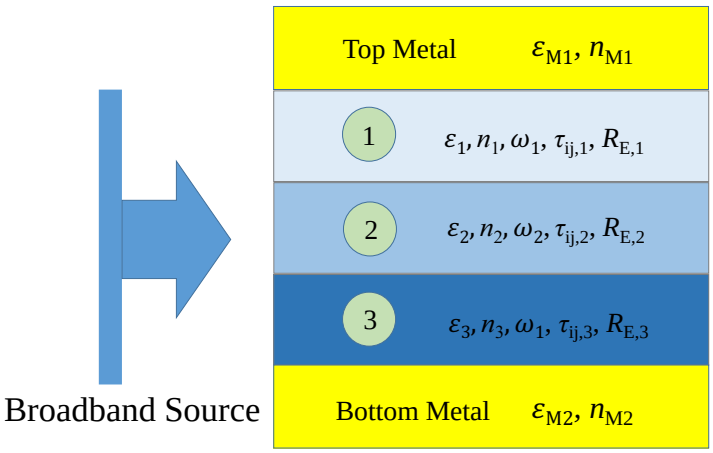

Figure 4.1: The schematic shows the variation of parameters for 2D FDTD simulation. Three gain mediums and cladding metals will have different refractive index and permittivity, which are given by creating material system database. The gain mediums will also have different center emission frequency, carrier lifetime and electrical pumping rate. These parameters are taken from Schrodinger-Poisson solver. a broadband source is used to produce emission of all possible frequencies of the system.

material parameters which compose the cavity.

In our proposed design, there are three gain mediums. Each gain medium will provide different gain for three types of emission. So, the Maxwell equation will be modified for three different gain medium as

$$\frac{n}{c}\frac{\partial E_{\pm}}{\partial t} = \mp\frac{\partial E_{\pm}}{\partial z} + (g_{i,1} + g_{i,2} + g_{i,3} - l)E_{\pm}. \tag{4.2}$$

Here, i can vary from 1 to 3, respectively for S_1, S_2, and S_3. It means that each emission will get different gain from each of the gain medium.

4.1.2 Gain Medium Modeling

The gain g comes from the laser gain medium. The laser gain medium is modeled using 4 level laser system model. The model implements the following set of equation

$$\frac{dN_3}{dt} = -\frac{N_3(1-N_2)}{\tau_{32}} - \frac{N_3(1-N_0)}{\tau_{30}} + \frac{J}{e} \tag{4.3a}$$

$$\frac{dN_2}{dt} = \frac{N_3(1-N_2)}{\tau_{32}} - \frac{N_2(1-N_1)}{\tau_{21}} \tag{4.3b}$$

$$\frac{dN_1}{dt} = \frac{N_2(1-N_1)}{\tau_{21}} - \frac{N_1(1-N_0)}{\tau_{10}} \tag{4.3c}$$

$$\frac{dN_0}{dt} = \frac{N_3(1-N_0)}{\tau_{30}} + \frac{N_1(1-N_0)}{\tau_{10}} - \frac{J}{e}. \tag{4.3d}$$

Here N_i is the electron population density in Level i and τ_{ij} is the decay time constant between levels i and j, J/e is the electrical pumping. For level 4, electrical pumping comes from current injected from the previous period and for level 0, current is injected to next period from it. The electron populations vary with pumping rate and spontaneous emission decay $(N_iN_j)/\tau_{ij}$. Electrons in Level 3 spontaneously decay to Levels 2 and 0 with decay time constants τ_{32} and τ_{30} respectively. Electrons in Level 2 spontaneously decay to Level 1 with decay time constants τ_{21}. The decay time constants and electrical pump rate are calculated from Schrodinger-Poisson solver.

The gain of the laser medium is calculated as

$$g = \sigma \omega_i \Delta N, \tag{4.4}$$

where σ is the gain cross section, ΔN is population inversion given by $\Delta N = N_2 - N_1$, and ω_i is the angular frequency of the corresponding emission. The gain cross-section is determined from the mode shape of emission in the cavity and ω_i is set by the energy level difference between level 1 and level 2, which is taken from the Schrodinger-Poisson solver.

The injected broadband emission consists light of all possible frequencies available in the mediums. But, only the frequencies within the gain spectrum defined by the four level system will experience gain in a specific gain medium. Other frequencies will not be amplified. So, the specific frequencies supported by specific gain medium, corresponding to their lasing level difference, will only have sufficient gain. So, S_1, S_2, and S_3 provide sufficient gain to ω_1, ω_2, and ω_3 respectively, which simulates the effect of lasing in the cavity. Now, if the gain is sufficient enough to overcome the losses introduced by the waveguide and other gain mediums, the emission will sustain in the cavity after few passes.

4.2 Waveguide Analysis and Design Optimization

We have calculated the response of the waveguides in the terahertz range, confinement of mode within the cavity. We also optimize the waveguide design on the

basis of threshold gain required for lasing.

4.2.1 Waveguide Response

Figure 4.2 shows the waveguide response for SI-SP waveguide, and Fig. 4.3 shows the response MM waveguides for both gold and copper cladding. We note that, for SI-SP waveguide, the output emission rapidly decreases in intensity below 5 THz. But for MM waveguide, we have emission over the 1–10 THz range. So, we choose to design MM waveguide for our proposed structure. From Fig. 4.3, we note that copper cladding provides better emission intensity for most frequencies in the simulation range.

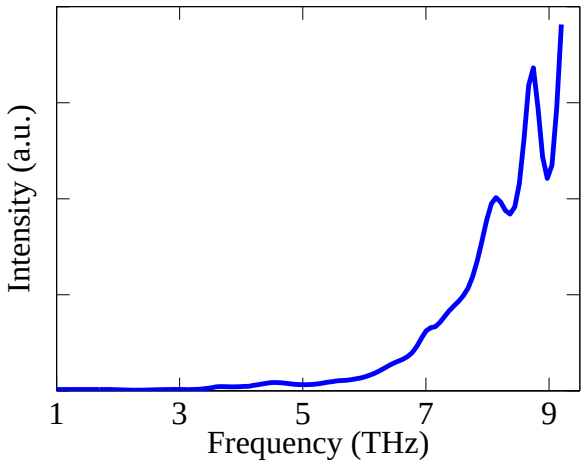

Figure 4.2: Response of Semi-insulating Surface Plasmon Waveguide.

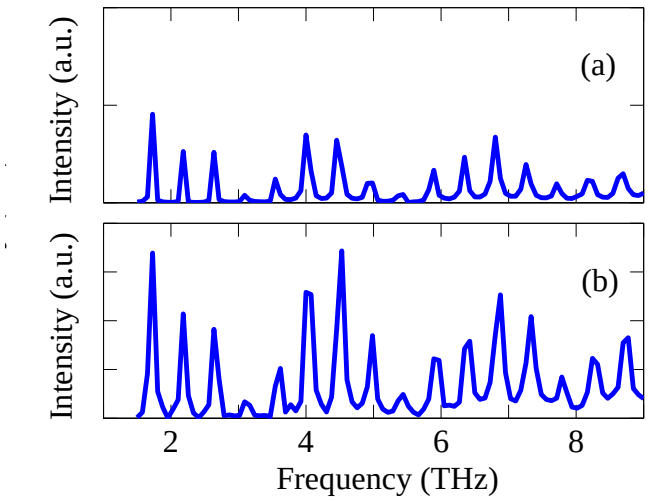

Figure 4.3: Response of Double Metal (MM) waveguide with (a) Gold cladding and (b) Copper cladding.

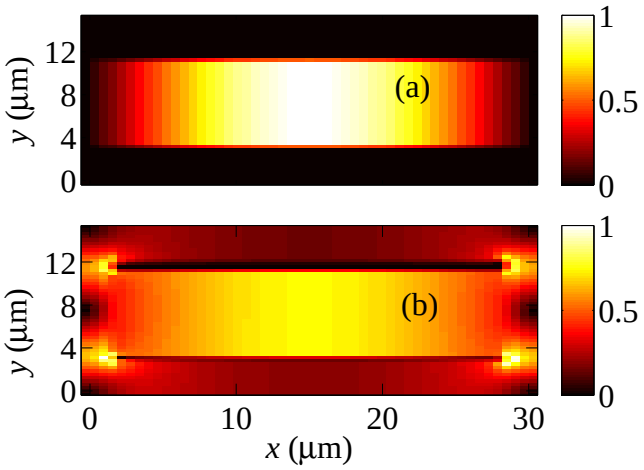

Figure 4.4: Confinement of mode inside Double metal Waveguide with (a) Metal and (b) Air boundary condition

4.2.2 Mode Profile Analysis

Mode confinement is very important to ensure low threshold gain in the QCL. The mode confinement within double metal waveguide with 30 μm transverse length and 10 μm width is shown in Fig. 4.4 with metal boundary condition and air

boundary condition. As we can see from the Fig. 4.4, for double metal waveguide with metal boundary, we can achieve excellent mode confinement, which will result in confinement factor very close to unity. We also note that, for air boundary conditions, the mode is not well confined within the cavity. It spreads outside of the laser cavity, which will result in decrease of confinement factor, and as a result the threshold gain will increase. We calculate the mode profiles of the emission, which will be supported by the waveguide structure.

Figures 4.5, 4.6, and 4.7 show the corresponding modes at the center frequencies of emission from S_1, S_2, and S_3, namely 1.7 THz, 4.3 THz, and 7.2 THz. We note that at 1.7 THz, there are only two supported modes, at 4.3 THz, there are 3 supported modes and at 7.2 THz, there are 5 supported modes in the waveguide. So, the number of supported modes, increases with increasing frequency, or decreasing wavelength. Though only those modes which get sufficient gain from the

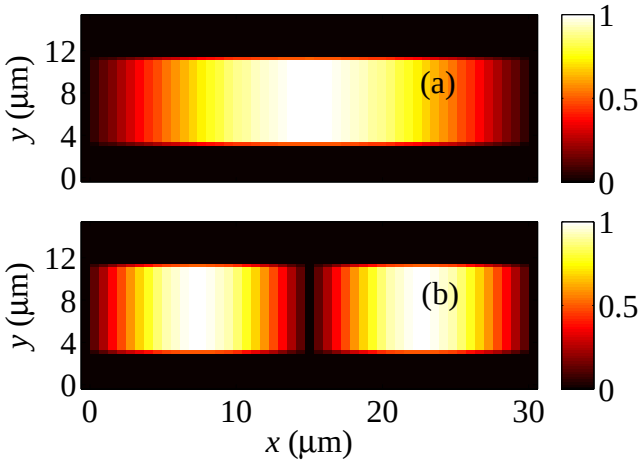

Figure 4.5: Mode profiles within the waveguide for 1.5 THz. Only two modes can exist at this frequency – (a) Mode 0 and (b) Mode 1.

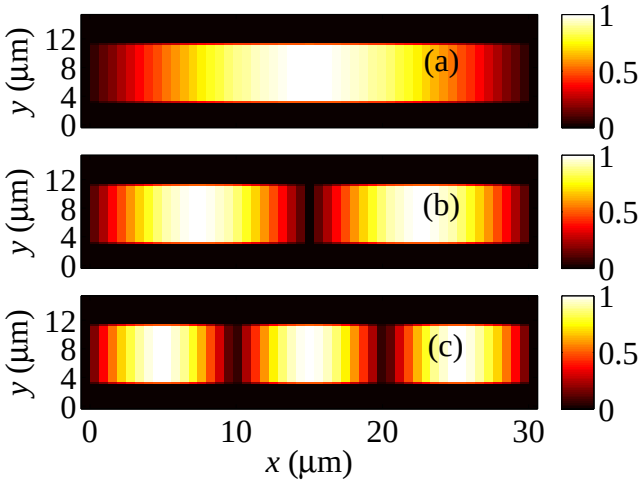

Figure 4.6: Mode profiles within the waveguide for 4.5 THz. Three modes can exist at this frequency – (a) Mode 0, (b) Mode 1, and (c) Mode 2.

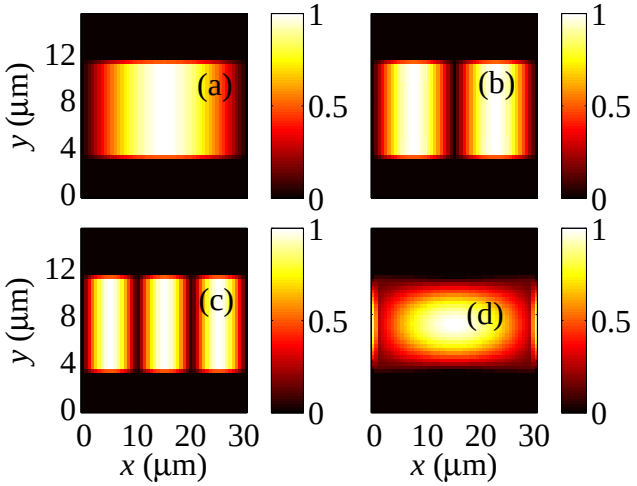

Figure 4.7: Mode profiles within the waveguide for 7 THz. Five modes can exist at this frequency (4 of them are shown) – (a) Mode 0, (b) Mode 1, (c) Mode 2, and (d) Mode 3

gain mediums will sustain in the cavity at the end.

To get further insight of the mode shape, we calculate the axial distribution and far field pattern of the modes for the limiting frequencies of the proposed struc-

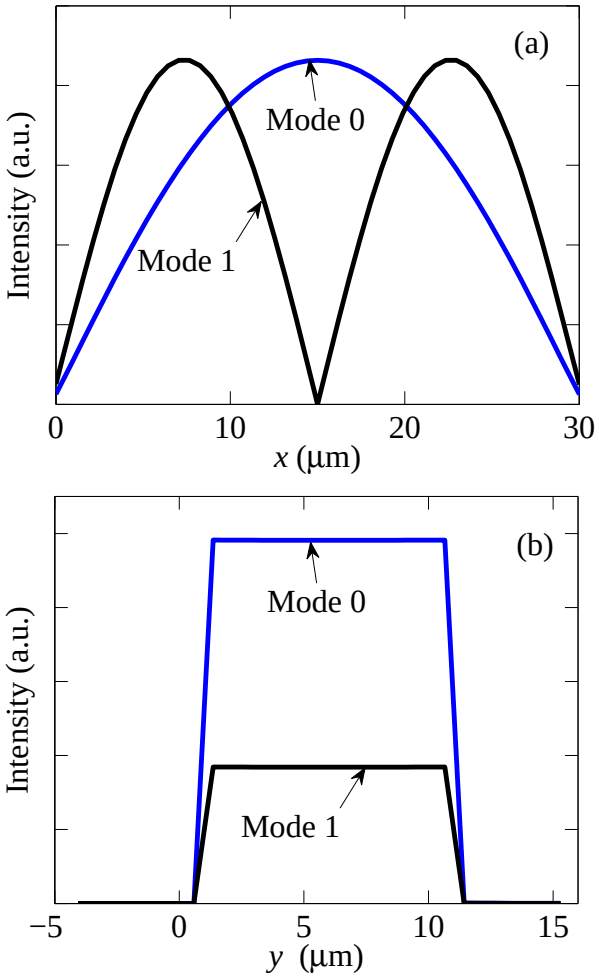

Figure 4.8: Distribution of mode profile in (a) x-axis and (b) y-axis at lowest attainable frequency 1 THz.

ture. Figures 4.8 and 4.9 shows the axial distribution of modes from 1 THz and 9 THz respectively. As we can see from the figures, the fundamental modes for both cases have Gaussian like distribution along x-axis and uniform distribution along y-axis of the waveguide and show the highest intensity among all available modes. Figure 4.10 shows the far field pattern for the two extreme frequencies. We note that, the 1 THz emission has a more spread out far-field pattern with a

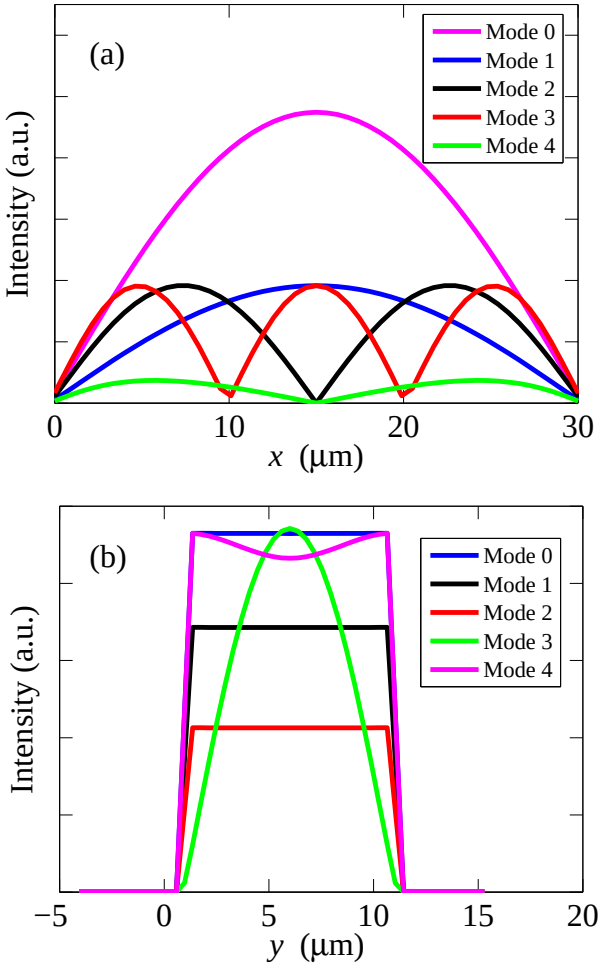

Figure 4.9: Distribution of mode profile in (a) x-axis and (b) y-axis at highest attainable frequency 9 THz.

lower intensity than 9 THz emission. The reason can be attributed to longer wavelength resulted from the lower frequency of 1 THz emission, which causes the emission to spread out more in the space.

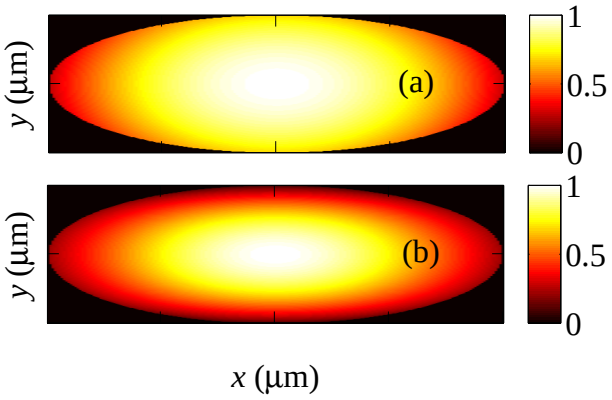

Figure 4.10: Far field distribution for limiting frequencies: (a) 1 THz and (b) 9 THz.

4.2.3 Threshold Gain Analysis

We have calculated the loss and threshold gain for MM waveguide for the traditionally used gold cladding MM waveguide and alternative copper cladding MM waveguide, which is shown in Fig. 4.11. Figure 4.11(a) shows that loss decreases with increasing frequency. This can be attributed to smaller wavelength due to increasing frequency results in better confinement. From 4.11(b), we note that the threshold gain decreases with increasing frequency. For both gold and copper the threshold gain for the whole 1–10 THz range is below the gain we have for the most of the emission in from our proposed structure. However, we note that copper cladding provides lower threshold gain than gold cladding, hence we choose to use copper cladding for our structure.

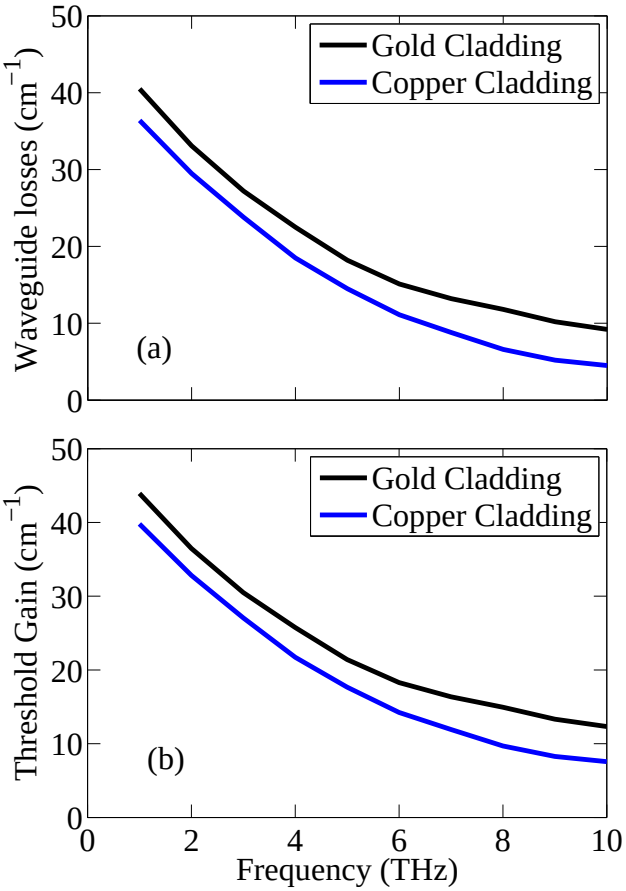

Figure 4.11: (a) Waveguide loss and (b) Threshold gain in double meal waveguide.

4.2.4 Parameter Optimization

Here, we will optimize the different design parameter for the waveguide that we will design. We already found that copper cladding will perform better than the traditional gold cladding. Now, we will optimize the core width of the active region and width of the metal claddings.

We have calculated the effect of active region width on the threshold gain. The response for 3 μm and 10 μm active region which is shown in Fig. 4.12. We note

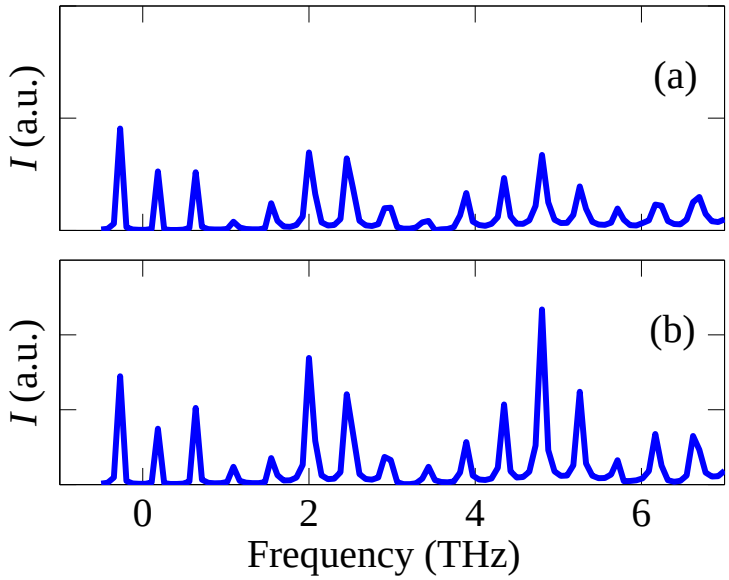

Figure 4.12: Output emission intensity (I) of double metal waveguide for (a) 3 μm and (b) 10 μm active region width

that for wider active region the response intensity of the emission increases. This can be attributed to better confinement of higher frequency emission in the cavity due to shorter wavelength. To optimize the active region width of the core, we have calculated the waveguide losses and threshold gain as a function of active region width. Figure 4.13 shows the variation of waveguide losses and threshold gain as active region width varies for two specific frequencies, 4 THz and 8 THz. We note that, for both frequencies, as the active region width increases, the waveguide loss decreases, and hence the threshold gain also decreases. The rate of decrease is slower around 10 μm range, and also it is difficult to grow wider active region using MBE technique [9], hence we choose an active region width of 10 μm.

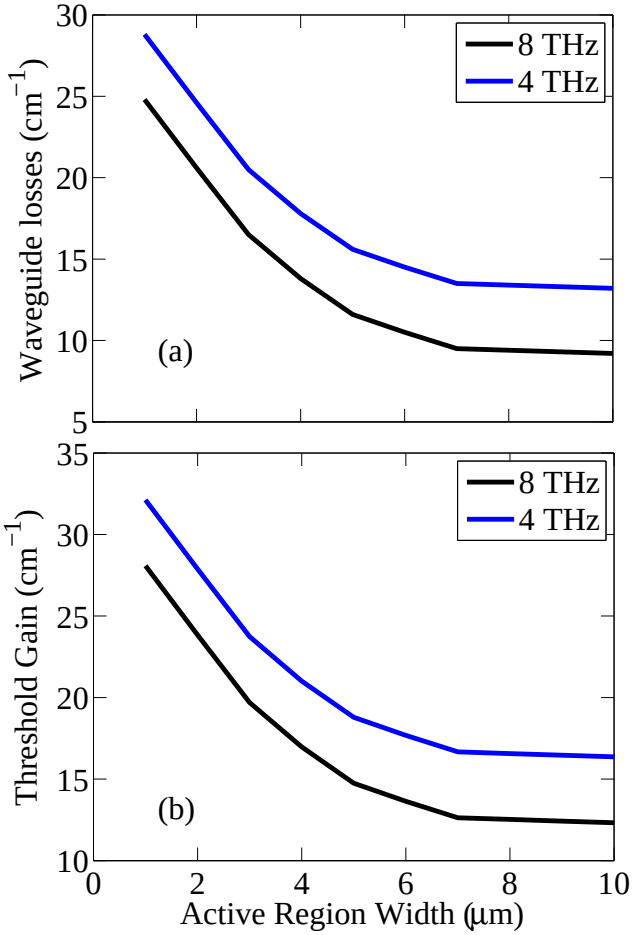

Figure 4.13: (a) Waveguide loss and (b) Threshold gain in double metal waveguide for active region width variation.

We have also observed the effect cladding width, which is shown in Fig. 4.14. We note that threshold gain decreases as the cladding width increases. But, threshold gain decreases up to increase of cladding width up to 1 μm, then there is no effect of increasing cladding width, as there will be no further improvement of confinement of light within the cavity. So we choose cladding width of 1 μm.

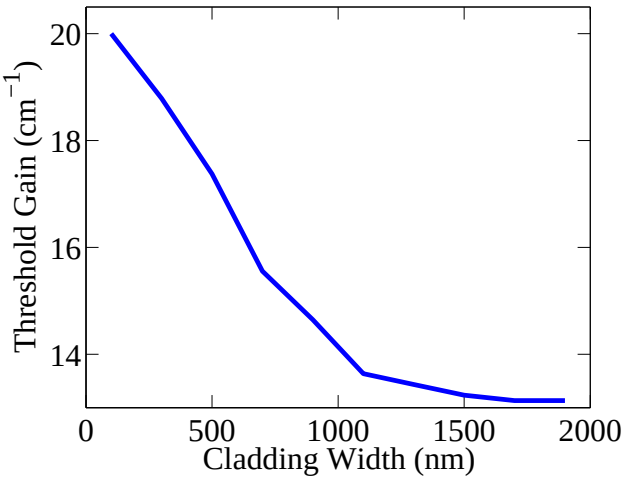

Figure 4.14: Threshold gain in double metal waveguide with metal cladding width variation.

4.2.5 Overall Performance

Finally, we have calculated the emission intensity for the optimized waveguide for all bias. Figure 4.15 shows the response of the optimized waveguide with the optimized parameters. The final emission intensity for the proposed waveguide design at 67 kV/cm bias is shown. The response of the waveguide for broadband input is also shown in the figure. We note that, all the three emission frequencies get sufficient gain from the core, which will result in a sustain emission from the laser.

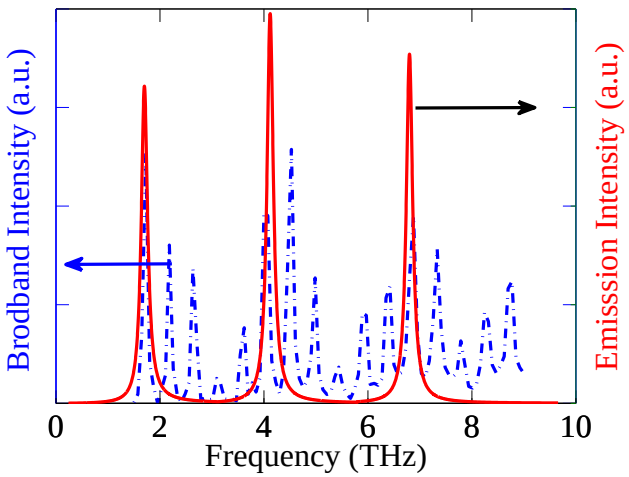

Figure 4.15: Response for optimized waveguide for broadband input, along with final emission from designed gain medium.

Chapter 5

Conclusion

Terahertz emission range is of significant importance due to numerous applications of this spectral range. But due to lack of suitable radiation source, historically, terahertz spectral range is extremely less explored. Among different alternative sources of terahertz emission, quantum cascade laser is the most promising. QCL provides the opportunity to control the output emission from design and hence makes it very suitable for a compact terahertz emission source. GaAs based terahertz QCLs up to 5 THz has already been reported. Comparatively new GaN based material system, provides the opportunity to explore terahertz emission beyond 5 THz, due to its much higher LO phonon resonance energy.

QCL also provides opportunity for hetero-active region emission, as pumping in QCL is sequential. Sequential pumping results in no competition for pumping energy, hence, multiple active region can simultaneously work together in a single laser cavity. So, multiple frequency emitting THz QCL is possible. Moreover, using various tuning techniques, it is possible to achieve each of the frequency to

be varied over a range. This will result in emission of broad range of terahertz range.

Here, we have proposed and analyzed ultra-broadband GaN based terahertz quantum cascade laser, which can cover a range of 1–10 THz using bias tuning technique. This range has significant application in spectroscopy and imaging. We have analyzed the electrical and optical properties of the proposed ultra-broadband QCL. We have calculated its gain spectrum and carrier transport. Hetero-structure devices inherently suffer from current mismatch assisted performance deterioration. We propose a method to find out the effect of current mismatch on the output emission. We find that current mismatch of more than 10% will result in severe decrease in gain, which will ultimately cease the emission. We provide the designed QCL with transitional collector region to contain the current mismatch withing 10% within the whole 1–10 THz range.

Waveguide design for terahertz emission is challenging, due to significantly longer wavelength than traditional mid-IR emission. We have analyzed the performances of alternative waveguides in the whole terahertz range emission of our proposed design. We show that double metal waveguide with copper cladding can support the broadband emission. We also provide optimization of waveguide parameters like core and cladding widths, to extract the best confinement and emission spectra for the broadband emission in the terahertz range. We explore the detail mode profile to analyze the performance of the waveguide.

In conclusion, we propose an ultra-broadband GaN based quantum cascade laser,

that can be used as a compact and high intensity source for the important terahertz emission range. We also develop detail theoretical modeling of the QCL, which can be used for analyzing performance of any terahertz GaN based QCL.

Bibliography

[1] A. Einstein, "Zur quantentheorie de strahlung," *Phy. Z.*, vol. 18, p. 121, 1917.

[2] T. H. Maiman, "Stimulated optical radiation in ruby masers," *Nature*, vol. 187, p. 493, 1960.

[3] A. Yariv, *Quantum Electronics*. Wiley, 1989.

[4] J. Wilson and J. F. B. Hawkes, *Optoelectronics - An Introduction*. Prentice Hall, 2001.

[5] R. F. Kazarinov and R. A. Suris, "Possibility of amplification of electromagnetic waves in a semiconductor with a superlattice," *Sov. Phys. Semicond.*, vol. 5, p. 707, 1971.

[6] J. Faist, F. Capasso, D. Sivco, C. Sirtori, A. Hutchinson, and A. Cho, "Quantum cascade laser," *Science*, vol. 264, p. 553, 1994.

[7] M. A. Talukder, "Analysis of self-induced transparency modelocking of quantum cascade lasers," Ph.D. dissertation, University of Maryland Baltimore County, 2010.

[8] F. Wei, "Review of terahertz semiconductor sources," *Journal of Semiconductors*, vol. 33, p. 03001, 2012.

[9] B. S. Williams, "Terahertz quantum-cascade lasers," *Nature Photonics*, vol. 1, pp. 517–525, 2007.

[10] K. V. et. al., "Broadly tunable terahertz generation in mid-infrared quantum cascade lasers," *Nature Communications*, vol. 4, p. 130617, 2013.

[11] J. R. Freeman, A. Brewer, J. Madeo, and P. Cavalie, "Heterogeneous thz quantum cascade lasers: Broadband operation," in *IEEE International Conference, Houston, TX*, 2011, pp. 1–2.

[12] S. P. Khanna, M. Salih, P. Dean, A. G. Davies, and E. H. Linfield, "Electrically tunable terahertz quantum-cascade laser with a heterogeneous active region," *Applied Physics Letters*, vol. 95, p. 181101, 2009.

[13] D. Turcinkova, "Ultra-broadband heterogeneous quantum cascade laser emitting from 2.2 to 3.2 THz," *Applied Physics Letters*, vol. 99, p. 191104, 2011.

[14] K. Vijayraghavan, Y. Jiang, M. Jang, and M. A. Belkin, "Broadly tunable terahertz generation in mid-infrared quantum cascade lasers," *Nature Communications*, vol. 4, p. 2021, 2013.

[15] H. Yasuda, T. Kubis, I. Hosako, and K. Hirakawa, "Design of terahertz quantum cascade lasers for high temperature operations using non-equilibrium green's function method," *PIERS Proceedings, Malaysia*, 2012.

[16] R. Colombelli, "Far-infrared surface-plasmon quantum-cascade lasers at 21.5 μm and 24 μm wavelengths," *Applied Physics Letters*, vol. 75, pp. 2620–2622, 2001.

[17] X. Yin, B. W.-H. Ng, and D. Abbott, *Terahertz Imaging for Biomedical Applications*. Springer, 2012.

[18] M. J. Fitch and R. Osiander, "Terahertz waves for communications and sensing," *Johns Hopkins APL Technical Digest*, vol. 25, p. 4, 2004.

[19] A. Gomez, N. Pere-Laperne, and L.-A. de Vaulchier, "Dark current analysis of quantum cascade detectors by magneto-resistance measurements," *Physical Review B*, vol. 72, p. 085307, 2008.

[20] M. Geiser, C. Pflügl, A. Belyanin, Q. J. Wang, N. Yu, T. Edamura, M. Yamanishi, H. Kan, M. Fischer, A. Wittmann, J. Faist, and F. Capasso, "Gain competition in dual wavelength quantum cascade lasers," *Opt. Express*, vol. 18, no. 10, May 2010.

[21] C. Sirtori, "Long-wavelength ($\lambda \sim 8$–11.5 μm) semiconductor lasers with waveguides based on surface plasmons," *Opt. Letters*, vol. 23, pp. 1366–1368, 1998.

[22] R. Kohler, "Terahertz semiconductor heterostructure laser," *Nature*, vol. 417, pp. 156–159, 2002.

[23] J. A. Fan, M. A. Belkin, and F. Capasso, "Wide-ridge metal-metal terahertz quantum cascade lasers with high-order lateral mode suppression," *Applied Physics Letters*, vol. 92, p. 031106, 2008.

[24] W. Terashima and H. Hirayama, "Intersubband spontaneous emission from GaN-based THz quantum cascade laser," *Proceedings of the SPIE*, vol. 8625, pp. 862 516–10, 2013.

[25] G. Suna, Richard, A. S. b, and J. B. Khurginc, "Active region design of a terahertz GaN/AlGaN quantum cascade laser," *Elsevier Superlattices and Microstructures*, vol. 37, 2005.

[26] H. Zhao, R. A. Arif, Y.-K. Ee, and N. Tansu, "Self-Consistent Analysis of Strain-Compensated InGaN-AlGaN Quantum Wells for Lasers and Light-Emitting Diodes," *IEEE Journal of Quantum Electronics*, vol. 45, 2009.

[27] A. Siegman, *Lasers*. University Science Books, 1986.

[28] H. C. Liu and F. Capasso, *Intersubband transitions in Quantum well*. Academic press, 2000.

[29] R. Ferreira and G. Bastard, "Evaluation of some scattering times for electrons in unbiased and biased single- and multiple-quantum-well structures," *Phys. Rev. B*, vol. 40, p. 1074, 1989.

[30] T. Unuma, M. Yoshita, T. Noda, H. Sakaki, and H. Akiyama, "Intersubband absorption linewidth in gaas quantum wells due to scattering by interface roughness, phonons, alloy disorder, and impurities," *J. App. Phys.*, vol. 93, p. 1586, 2003.

[31] A. Wittmann, Y. Bonetti, J. Faist, E. Gini, and M. Giovannini, "Intersubband linewidths in quantum cascade laser designs," *Appl. Phys. Lett.*, vol. 93, p. 141103, 2008.

[32] D. Indjin, P.Harrison, R. Kelsall, and Z. Ikonic, "Self-consistent scattering theory of transport and output characteristics of quantum cascade lasers," *Journal Of Applied Physics*, vol. 91, 2002.

[33] I. Vurgaftman and J. R. Meyer, “Band parameters for nitrogen-containing semiconductors,” *J. Appl. Phys*, vol. 94, 2003.

[34] O. Ambacher, J. Majewski, C. Miskys, A. Link, and M. Hermann, “Pyroelectric properties of Al(In)GaN/GaN hetero- and quantum well structures,” *J. Phys.: Condens. Matter*, vol. 14, 2002.

[35] E. Baumann, “Near infrared intersubband absorption and photovoltaic detection in GaN/AlN multi quantum well structures,” Ph.D. dissertation, Univ. of Neuchatel, 2007.